

Unveiling the Electrochemical Versatility of N-Doped Porous Carbon in Aqueous and Redox Additive Electrolytes

Karnan Manickavasakam, Rajashree Samantray, Mohammed A. Al-Huri, Vaishak Sunil, Izan Izwan Misnon, Jiaqian Qin,* and Md. Abdul Aziz*

Supercapacitors are prized for their high-power delivery, though their energy storage capacity is generally lower than that of batteries. A novel one-pot strategy for synthesizing nitrogen-doped porous carbon derived from KOH and urea-activated wheat bread waste (*Triticum aestivum*) is presented. This unique synthesis simultaneously achieves chemical activation and nitrogen doping in a single-step process, offering a cost-effective and scalable route for high-performance electrode materials. The supercapacitive properties of bread waste-derived activated carbon (BWC-700) in a 1 M H₂SO₄ aqueous electrolyte are investigated, with 0.01 M hydroquinone (HQ) acting as a redox-active agent. Morphological analysis via field-emission scanning electron microscopy confirms the material's hierarchical porous structure.

The (BWC-700) exhibits a specific capacitance of 486 F g⁻¹ at a current density of 1 A g⁻¹ in a half-cell configuration, with specific capacities of 1422 C g⁻¹ and 904 C g⁻¹ in three- and two-electrode systems, respectively. When HQ is incorporated into the electrolyte, the AC demonstrates excellent cyclic stability, retaining 82% of its capacitance after 5000 cycles. Notably, BWC-700 achieves a peak energy density of 56.5 Wh kg⁻¹, outperforming symmetric supercapacitors. These findings underscore the novel combination of waste valorization, green synthesis, and redox-enhanced energy storage, making this work highly relevant and competitive in the rapidly evolving field of supercapacitors.

1. Introduction

Growing energy demand due to rapid urbanization, climate change, and a shortage of natural resources are major challenges to the budding renewable green energy demands.^[1–3] This evolution is causing a rapid shift from the minimization of fossil fuels to electrified systems. The growing technology is driving researchers to look for better alternatives to green energy in

terms of new materials with cheaper costs and abundant availability.^[4] They have acquired significance in supercapacitors due to their extended cyclability, durability, and high-power output, making them a preferred choice over capacitors and batteries.^[5–9] Supercapacitors are segregated into two major categories based on their energy storage mechanism: electrical double-layer capacitors (EDLCs) and pseudocapacitors (PCs). The effectiveness of supercapacitors is greatly affected by the characteristics of the

K. Manickavasakam, M. A. Al-Huri
Interdisciplinary Research Center for Construction and Building Materials
King Fahd University of Petroleum and Minerals
Dhahran 31261, Saudi Arabia

R. Samantray
New Material Development
Amara Raja Energy & Mobility
Tirupati, Andhra Pradesh 517507, India

V. Sunil, I. I. Misnon
Center for Advanced Intelligent Materials
Universiti Malaysia Pahang Al-Sultan Abdullah
26300 Gambang, Malaysia

V. Sunil, I. I. Misnon
Faculty of Industrial Sciences and Technology
Universiti Malaysia Pahang Al-Sultan Abdullah
26300 Gambang, Malaysia

J. Qin
Department of Materials Science
Faculty of Science
Chulalongkorn University
Bangkok 10330, Thailand
E-mail: jiaqian.q@chula.ac.th

J. Qin
Center of Excellence in Responsive Wearable Materials, Metallurgy and Materials Science Research Institute
Chulalongkorn University
Bangkok 10330, Thailand

M. A. Aziz
Interdisciplinary Research Center for Hydrogen Technologies and Carbon Management
King Fahd University of Petroleum and Minerals
Dhahran 31261, Saudi Arabia
E-mail: maziz@kfupm.edu.sa

M. A. Aziz
Department of Civil & Environmental Engineering
King Fahd University of Petroleum & Minerals
Dhahran 31261, Saudi Arabia

 Supporting information for this article is available on the WWW under <https://doi.org/10.1002/batt.202500342>

active electrode materials.^[10–14] Energy-related materials with potential for use in EDLCs include carbon nanotubes, carbon nanofibers, and graphene-like carbon obtained from biomass.^[15–18] Conversely, pseudocapacitive behavior predominantly involves materials like metal oxides, metal hydroxides, and conducting polymers.^[19] These materials facilitate redox reactions during the charging and discharging processes.^[20–22] Hybrid capacitors combine both EDLC and PC materials, permitting both chemical redox reactions and physical adsorption of ions at the electrode–electrolyte interface.^[23,24]

Although hybrid and PC-based materials offer outstanding performance, EDLCs are favored due to their cost-effectiveness, wide availability, and nontoxic properties. Activated carbon (AC), frequently obtained from carbonaceous biomass because of its cost-effective manufacturing processes, is a prevalent choice for commercial supercapacitors.^[25,26] Moreover, carbonaceous biomass is considered a preferable source for AC synthesis, taking into account environmental concerns, in contrast to fuel or coal-based precursors.^[27–29] Various carbons derived from biomass exhibit potential for use in supercapacitors, contributing to the development of sustainable and efficient energy storage solutions. These carbons include rice husk,^[30] straw,^[31] cauliflower,^[32] aloe vera,^[33] corn cob,^[34] coconut shell,^[35] lignin,^[36] orange peel,^[37] date seed,^[38] spent mushroom,^[25] litchi seed,^[39] and brinjal waste.^[40]

Triticum aestivum (bread wheat waste) offers numerous benefits as a precursor for AC production. It stands out among biomass sources that have been extensively studied for their potential in supercapacitor applications due to its nitrogen content and high carbohydrate composition that have not been fully utilized yet in this field of research. Its soft texture and inherent nitrogen content provide a chance for carbonization and direct N doping processes which make it a versatile option as a precursor material, for energy storage applications. The above-mentioned factors make bread waste a suitable candidate for the supercapacitor application. The porous properties of the material, specific capacitance, and specific surface area of a supercapacitor are the main factors that influence its capacitance to store charge.^[41,42] Attaining a substantial specific surface area is crucial for organizing carbon in an optimal manner, and this is typically achieved through the activation process.^[43–45] Chemical activation and physical activation are the two main methods, with the straightforward and effective approach of producing highly porous AC from biomaterials through chemical activation.^[46,47] Enhancing cell voltage and specific capacitance is a significant challenge when using supercapacitors in practical applications. Increasing the specific capacitance of ACs by incorporating heteroatoms like boron, nitrogen, oxygen, or sulfur into the carbon matrix is one workable solution to this problem.^[48,49] This doping enhances the electrical conductivity of the ACs, thereby contributing to an elevation in the specific capacitance of supercapacitors. Heteroatoms play a vital role in elevating pseudocapacitance and improving the wettability of the pore surface, ultimately reducing obstacles to charge transfer.^[50] N-doping serves as a specialized approach that has been extensively utilized for this purpose to improve the surface area, and conductivity with

improved active sites, and interlayer distance. This method proves particularly effective in maximizing supercapacitor performance by optimizing the structure and properties of the AC material, leading to improved energy storage capabilities.^[51,52] Elevating the cell voltage of supercapacitors represents a significant hurdle in their advancement, constituting another major challenge. This objective can be accomplished by employing diverse electrolytes, which include ionic liquids, non-aqueous electrolytes, and aqueous electrolytes containing redox additives. Redox-active species play a crucial role in engaging with electrodes and electrolytes, thereby contributing to the broadening of the potential window for supercapacitors.^[53] Redox additives offer several advantages in addressing this challenge.^[54] Firstly, they are more cost-effective compared to other electrolytes. Moreover, the processing of redox additives can be conducted at room temperature during the manufacturing process, rendering them a practical and cost-efficient choice for augmenting the cell voltage of supercapacitors.^[47] The capability to function at higher cell voltages introduces new possibilities for enhancing the energy density and overall performance of supercapacitors, positioning them as more competitive options across various applications within the realm of energy storage.^[55] Limited research has focused on examining how biomass-derived ACs perform when combined with electrolytes in a coordinated manner until now. This study stands out by assessing the use of carbon sourced from bread waste, showcasing an increase in energy density, highlighted as a step forward, in the effective application of redox additives.

Recent research findings showcase significant advancements in supercapacitor technology. One notable example is an organic redox additive incorporated hydrogel that shows excellent performance in a high energy density supercapacitor with 77.6% retention of capacitance over 10,000 charge and discharge cycles.^[56] This hydrogel redox-based redox additive shows an exceptional specific capacitance of 642 F g^{-1} at a 0.5 A g^{-1} current density and achieves a high energy density of 12 Wh kg^{-1} . By the same way, Suman et al.^[57] successfully developed a reduced graphene oxide based symmetric supercapacitor utilizing $0.05 \text{ M K}_4[\text{Fe}(\text{CN})_6]$ in $0.5 \text{ M K}_2\text{SO}_4$ as a redox additive. This innovative design exhibits an excellent specific capacity and an improved 36.8 Wh kg^{-1} energy density and shows an improved 134% retention in capacitance over 5000 long cycles. Additionally, kapok fiber-derived 2D biocarbon nanosheet^[58] with an enhanced surface area of $\approx 3359.2 \text{ m}^2 \text{ g}^{-1}$ achieved good performance in potassium ferri- and ferrocyanide-based redox additives. In a similar vein, Gang et al. reported self-healing redox-mediated gel polymer electrolytes such as polyacrylic acid/polyisodecyl methacrylate/ $\text{K}_3[\text{Fe}(\text{CN})_6]$. Based on the observed results this self-healing-based supercapacitor device shows a tremendous specific capacitance of 271.6 mF cm^{-2} with an energy density of $98.1 \mu\text{Wh cm}^{-2}$.^[59] Lastly, using a $1 \text{ M Na}_2\text{SO}_4$ electrolyte for novolac-based porous carbon, Kruner et al. recorded a capacitance of almost 127 F g^{-1} .^[60] This capacitance was further elevated to a specific energy of $\approx 33 \text{ Wh kg}^{-1}$ with the incorporation of a 6 M KI redox additive. Numerous efforts have been directed toward investigating redox mediators and their impact

on enhancing electrochemical properties through the incorporation of porous carbon. However, there aren't many studies on the one-pot synthesis of porous carbons and how they behave electrochemically in redox and aqueous electrolytes for supercapacitor applications.^[44]

The research adopts a one-pot method to create AC from wheat bread waste biomass, specifically *Triticum aestivum*. The high nitrogen level of urea makes it a good choice for making nitrogen-doped carbon-based products. It is envisaged that the direct utilization of urea will result in the production of novel compositions and lead to an improvement in AC for applications involving energy storage. The method is mainly distinguished by its cost efficiency and employs a single-pot, single-step synthesis approach during the activation process. This simplified one-pot strategy reduces the complexity of the process. Also manages to activate chemicals and introduce nitrogen at the same time in a single step.

Notably, the use of a single-step chemical activation procedure involving KOH and urea from bread-derived biowaste at temperatures of 700, 800, and 900 °C is explored. The resulting AC is evaluated in electrolytes that are based on redox additives and in aqueous solutions. In an initial assessment using a two-electrode cell in 1 M H₂SO₄, a specific capacitance of 343 F g⁻¹ is generated, corresponding to a 17.15 Wh kg⁻¹ energy density. Particularly when redox additives like hydroquinone (HQ) are mixed with 1 M H₂SO₄, the specific energy increases dramatically. Under these circumstances, the AC exhibits a remarkable 904 C g⁻¹ specific capacity and a 56.5 Wh kg⁻¹ specific energy. The microporosity of the AC and the efficient migration of electrolyte ions into the carbon matrix is responsible for the exceptional electrochemical performance. It is noted that redox additive electrolytes yield energy that is more than 3.3 times greater than that of aqueous electrolytes. This underscores the potential of utilizing redox additive electrolytes to enhance the energy storage capabilities of the AC derived from bread biomass.

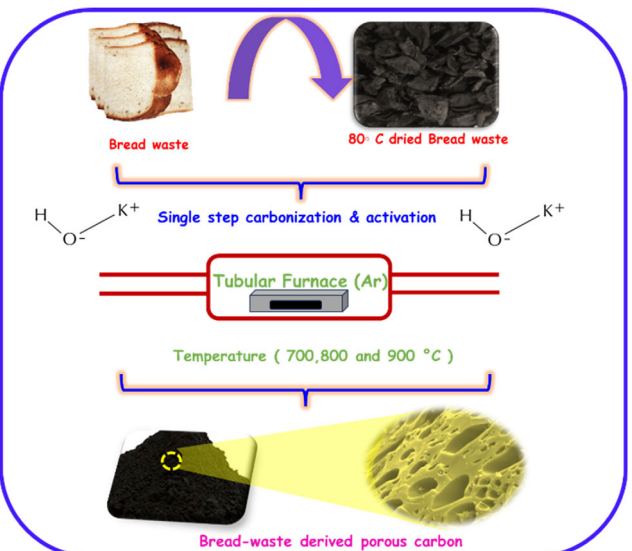
2. Experimental Section

2.1. Materials and Reagents

The material analysis, in terms of surface morphology, instrument usage, and electrochemical analysis, is delivered in the electronic Supporting Information.

2.2. Synthesis of N-Doped Bread Biomass Carbon

A meticulous cleaning process was conducted on the wheat bread waste samples sourced from a nearby supermarket to eradicate any dust or contaminants. After collection, they were sun-dried for 24 h, cut into small pieces, washed multiple times, and finally dried for 96 h at 80 °C to ensure complete drying. The dried samples were then crushed using an agate mortar, followed by chemical treatment with KOH and urea. The bread waste powder,



Scheme 1. Depicts the production process of AC derived from bread biomass waste. This involves a single-step activation process using KOH and urea at a temperature of 700–900 °C under inert conditions. KOH serves as the base activating agent, with urea being introduced to enhance pore development and leverage surface improvements in the porous carbon.

KOH, and urea were used maintaining a 1:3:2 ratio. It was further heated in an argon environment tubular furnace for 1 h at 700–900 °C was shown in **Scheme 1**. Another sample underwent treatment with KOH while maintaining a chemical ratio of 1:3, excluding urea activation. A hierarchical configuration of highly porous AC infused with nitrogen was produced through the single-step activation process utilizing bread waste. "Bare carbon" referred to unprocessed bread scraps. In this investigation, the porous carbon samples heated to 700, 800, and 900 °C with KOH and urea were designated as BWC-700, BWC-800, and BWC-900, respectively.

3. Results and Discussion

3.1. Morphological Characterization

The field-emission scanning electron microscopy (FE-SEM) images of bare carbon at different magnifications are shown in **Figure 1a,b** indicating a smooth carbon surface without active sites. In contrast, the BWC-700 sample shown in **Figure 1c,d** has an extremely porous surface structure, with macropores that range in size from several microns to 500 nm. Due to the sample's high specific surface capacitance, its porous surface plays a significant role in enabling ions with charge storage capacity.^[37]

3.2. Physiochemical Characterization

X-ray diffraction (XRD) of (**Figure 2a**) BWC-700 resembles two significant peaks observed within the range of 23.6°–42.5°, corresponding to the (002) and (100) planes, suggesting the existence of amorphous graphitic carbon.^[61] These outlines

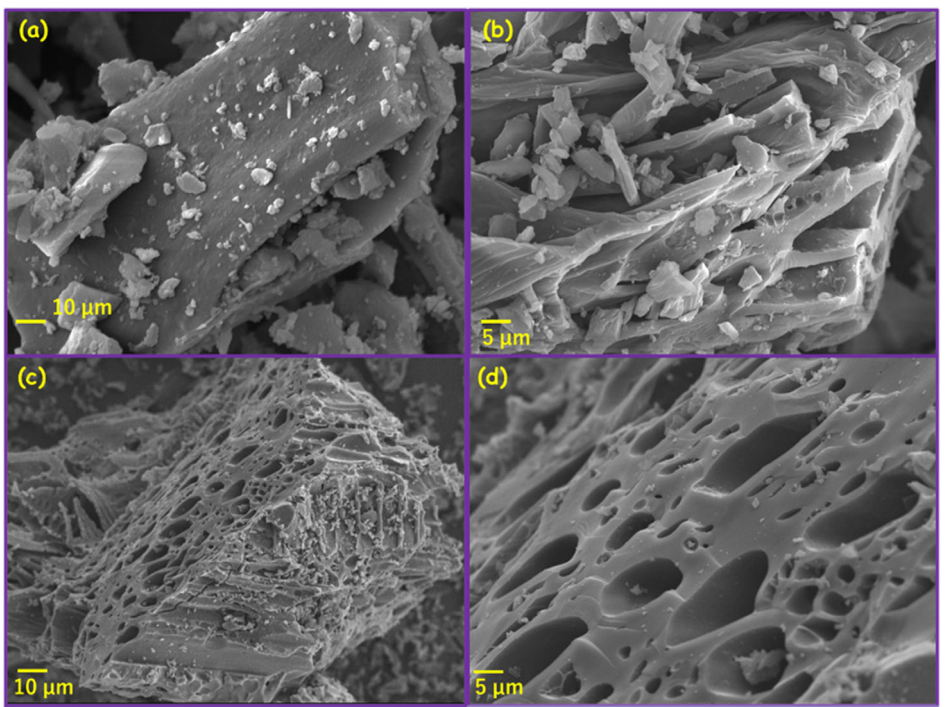


Figure 1. a,b) Displays FE-SEM images of bare carbon, while c,d) showcases FE-SEM photographs of BWC-700.

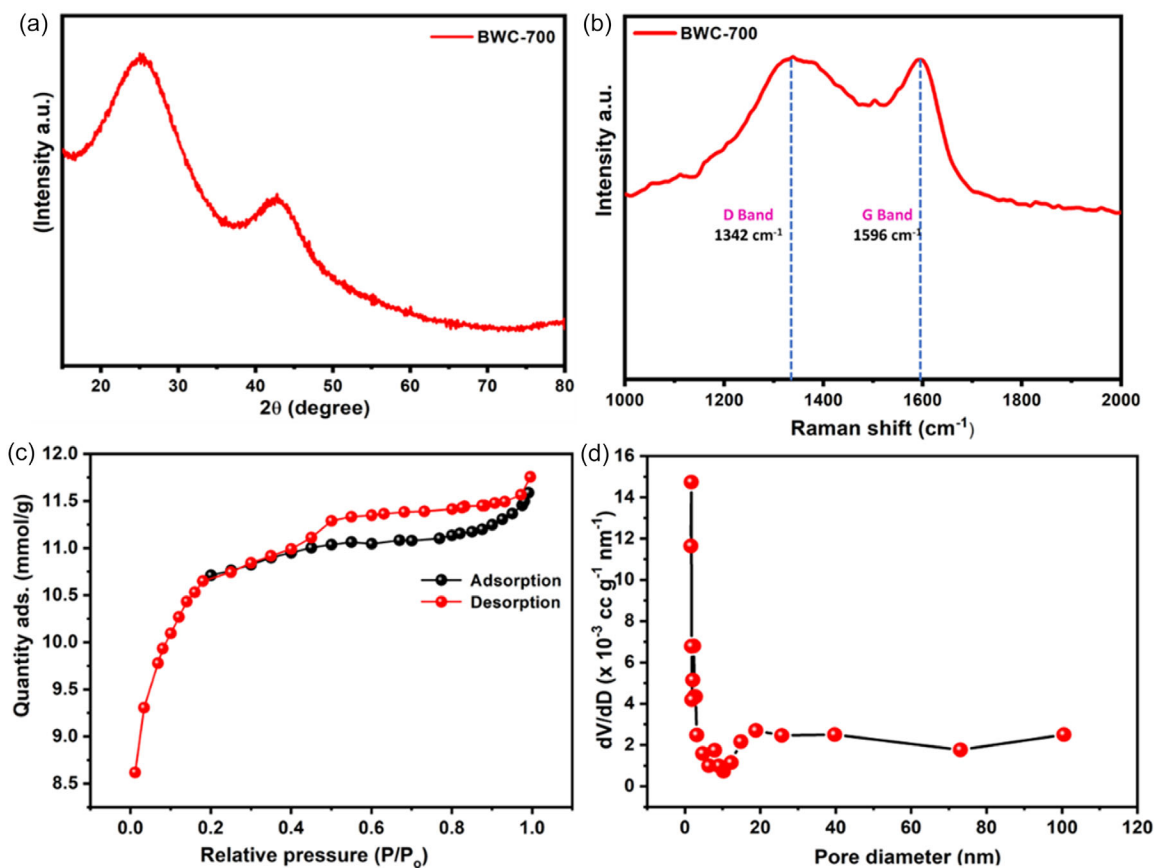


Figure 2. a) Displays the BWC-700 XRD analysis and b) shows the BWC-700 Raman spectrum. c) Shows the nitrogen adsorption/desorption isotherm and d) depicts the pore-size distribution of BWC-700.

illustrate how the chemical activation process involving KOH + Urea transforms bare carbon into AC. Fourier transform infrared spectroscopy, a reliable method for identifying functional groups in the carbon framework, defines the presence of oxygen and nitrogen functional groups on the BWC-700 material (Figure S1, Supporting Information). The hydroxyl group and the olefinic bond stretching vibration are connected to the infrared bands that range from 3480 to 1580 cm⁻¹. These bands show that sp² hybridized graphitic carbon with oxygen-containing functions is made during the KOH activation process.

Raman spectra displayed in Figure 2b exhibit the D and G bands at 1342 and 1596 cm⁻¹, respectively, with the calculated I_D/I_G value for BWC-700 being 0.84 (<1). Similarly, for bare carbon material, (Figure S2, Supporting Information) D and G bands range from 1590 and 1360 cm⁻¹, which results in the I_D/I_G ratio of 1.17 (>1). This indicates that the lower graphitic nature of the synthetic AC and the fewer faults that emerge are caused by high-temperature activation. BWC-700 displays a superior specific surface area of 850 m² g⁻¹ and a pore volume of 0.40 cc g⁻¹, as indicated by the BET isotherm compared to BWC-800 and BWC-900 (Figure S3, Supporting Information). The nitrogen adsorption/desorption isotherm (Figure 2c) showcases a Type IV isotherm with mesopores distributed across the carbon surface. BWC-700 possesses a larger number of mesopores rather than a few microporous carbons spread on the surface. Here, we have

calculated the pore size distribution (Figure 2d) of the sample using the density functional theory method and compared the BET surface area analysis for BWC-800 and BWC-900 samples. Due to the enhanced surface area compared to BWC-800 and BWC-900 (Table S1, Supporting Information), the substantial pore volume of BWC-700 facilitates the increasing specific capacitance. The sample's elemental components and functional groups were studied using X-ray photoelectron spectroscopy (XPS). O1s, N1s, and C1s peaks are visible at 532, 400, and 283 eV in the BWC-700 XPS survey spectrum (Figure 3a). According to this survey spectrum C and O atoms as well as N-doped hetero atoms are present throughout the BWC-700 sample (Figure 3b). According to their binding energy values, C i) at 284.4 eV (C—O), C ii) at 285.2 eV (C—N), C iii) at 286.2 eV (C—C), and C iv) at 289.1 eV (C=O), respectively, different carbon moieties are distinguished.^[62,63] (Figure 3c) illustrates the O 1s spectra analysis with the existence of three different forms of oxygen at O i) 531.3 eV, O ii) 532.4 eV, and O iii) 533.4 eV. These forms of oxygen provide information about the oxygen functionalities within BWC-700.^[33,64] (Figure 3d) signifies the BWC-700 N 1s peak with three merged peaks such as i) pyridinic-N (398.4 eV), ii) pyrrolic-N (399.4), and iii) graphitic N (400.3 eV), correspondingly.^[65] The graphitic-N layer on the carbon surface improves electrical conductivity and cyclic stability performance.

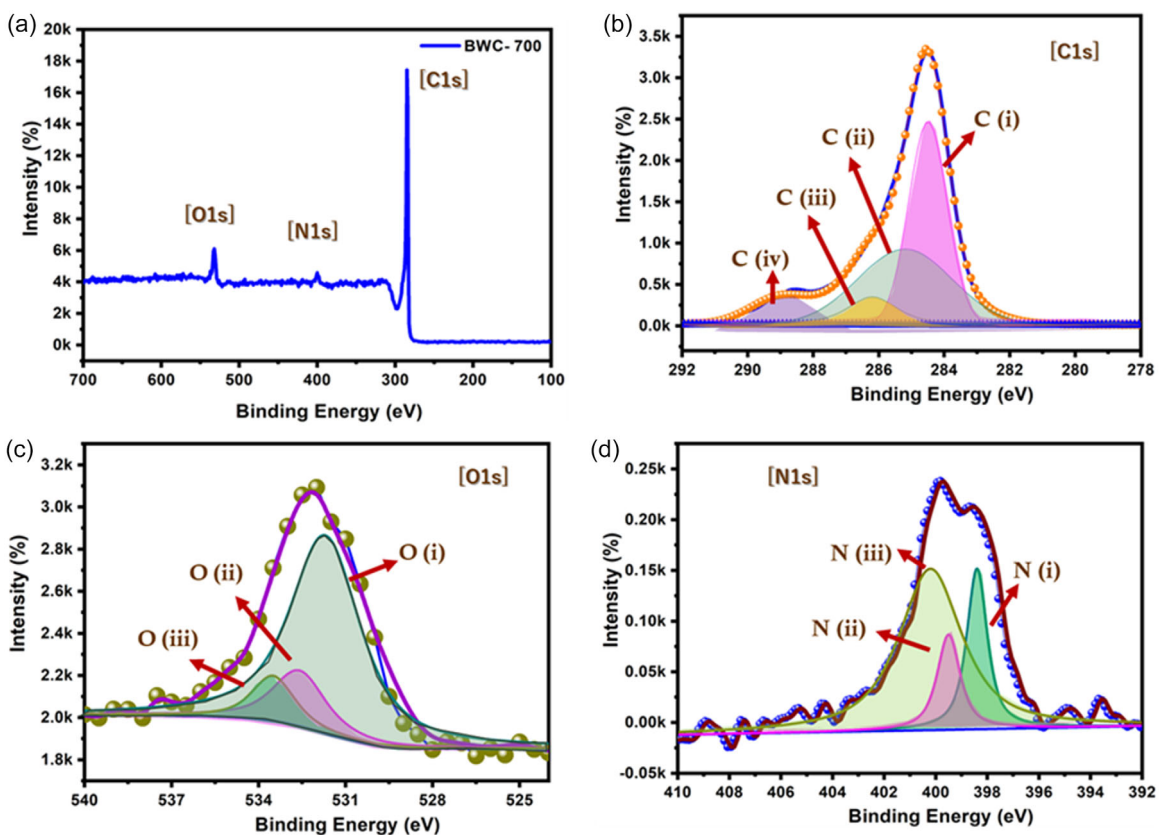


Figure 3. a) Illustrates the BWC-700 XPS survey spectrum while b) BWC-700 XPS spectra of C 1s. c) Showcases the BWC-700 XPS spectra of O 1s and d) presents the BWC-700 XPS spectra of N 1s.

3.3. Electrochemical Evaluation of a Three-Electrode Cell in Aqueous 1 M H₂SO₄

Figure S4a, Supporting Information depicts the cyclic voltammogram (CV) profile of BWC-700, bare carbon material, and bare current collector. BWC-700 demonstrates enhanced capacitance behavior compared to bare carbon and bare current collector. It is mainly due to oxonium ions formation on the carbon surface during electrochemical reaction and the existence of surface functionalities interaction in the 1 M H₂SO₄ solution. BWC-700 in Figure S4b, Supporting Information demonstrates a longer discharge time than the electrode with bare carbon, resulting in a specific capacitance of 486 F g⁻¹ for BWC-700 and 78 F g⁻¹ for bare carbon at a 1 A g⁻¹ current density. As a result, BWC-700 is chosen as the primary electrode for subsequent investigations in half-cell and full-cell studies. In half-cell experiments, BWC-700 is considered as the working electrode, with platinum mesh and Hg/Hg₂SO₄ acting as the counter and reference electrodes, respectively. The quasirectangular peaks in the CV curves of BWC-700, BWC-800, and BWC-900 at various sweep rates (Figure 4a) indicate reversible reaction occurs during the electrochemical reaction. The electrochemical window is primarily influenced by the composition of the reference electrode, electrolyte, and electrode materials. The galvanostatic charge-discharge (GCD) profiles (Figure 4b) for BWC-700, BWC-800, and BWC-900 at 1 A g⁻¹ reveal superior performance for BWC-700 with a specific capacitance of 486 F g⁻¹. The FE-SEM analysis of BWC-800 and BWC-900 (Figure S5, Supporting Information) clearly indicates a consistent porous nature, marked by nonuniform porosity and a

reduced specific surface area. Consequently, this hampers the specific capacitance of the sample in contrast to the BWC-700 electrode. The CV curves for BWC-700 at different scan rates (Figure 4c) show quasirectangular peaks, attributed to the presence of heteroatoms and oxonium ions on the carbon surface matrix.^[66] The specific capacitance at increasing current densities (Figure 4d) demonstrates BWC-700's outstanding rate capability, achieving 77% at 5 A g⁻¹. The comparison of specific capacitance observed over BWC-700, BWC-800, and BWC-900 electrode materials is presented in Figure 4e, confirming the remarkable electrochemical characteristics and high efficiency of the AC derived from BWC-700. Activation without urea, shown in Figure S6, Supporting Information, yields lower specific capacitance than BWC-700, further emphasizing the latter's potential for full-scale applications.

The Nyquist plot presented in Figure 4f for BWC-700, BWC-800, and BWC-900 in 1 M H₂SO₄ demonstrates a low R_{ct} value of 0.65 Ω for the BWC-700 electrode. The electrochemical impedance spectroscopy (EIS) curves were fitted with an equivalent circuit comprising different R and C components, as depicted in the inset of Figure 4f. This suggests BWC-700 electrode shows exceptional energy storage performance compared to all others used subject to the acidic electrolyte.

3.4. Electrochemical Evaluation of Full Cell in Aqueous 1 M H₂SO₄

To assess the possible suitability of BWC-700 in a 1 M H₂SO₄ aqueous electrolyte, a symmetric cell arrangement was established.

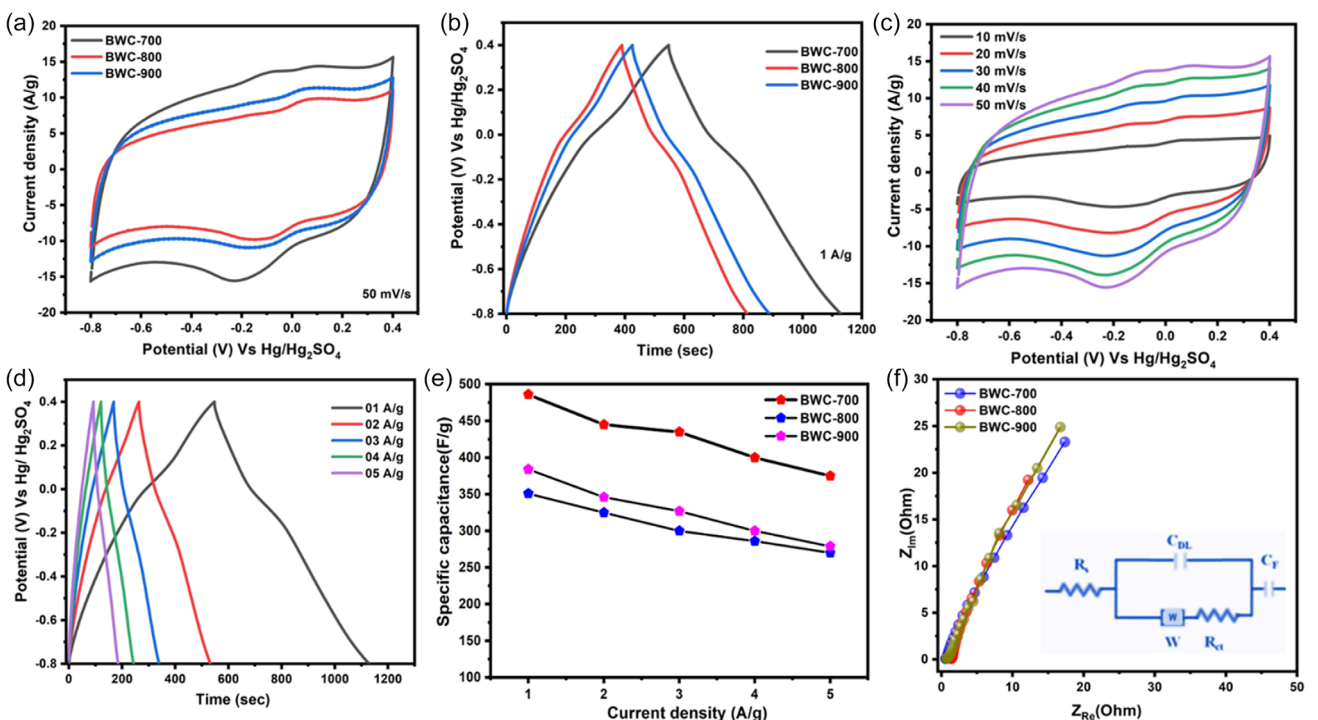


Figure 4. Displays various profiles and spectra related to the BWC-700, BWC-800, and BWC-900 electrodes. These include a) CV profiles at a 50 mV s⁻¹ scan rate, b) GCD profiles at a 1 A g⁻¹ current density, c) CV profiles of BWC-700 at different scan rates, d) CD profiles of BWC-700 at different current densities, e) specific capacitance plotted against current densities for BWC-700, BWC-800, and BWC-900, and f) EIS spectra for BWC-700, BWC-800, and BWC-900 electrodes and fitted equivalent circuit (inset).

This cell can only operate between 0.0 and 1.2 V in an aqueous electrolyte containing 1 M H₂SO₄. The CV curve in Figure 5a forms a rectangular shape, which clearly illustrates the electrode material's capacitive behavior. Typically, carbon-based symmetric supercapacitors in aqueous electrolytes have a working voltage of 1.2 V due to water decomposition occurring at 1.23 V in such electrolytes. Figure 5b illustrates the maximum electrode potential, at 0.8–1.2 V range in the CV at a constant scan rate of 50 mV s⁻¹. The GCD profile of BWC-700 demonstrates an enlarging C_{sp} of 343 F g⁻¹ at a 1 A g⁻¹ current density, as depicted in Figure 5c. As seen in Figure 5d, the specific capacitance, however, diminishes to 306, 286, 261, and 254 F g⁻¹, respectively, when the current rates vary from 2, 3, 4, and 5 A g⁻¹. The cyclic performance of BWC-700 electrodes was evaluated by subjecting them to 15,000 GCD cycles, as depicted in Figure 5e. Remarkably, the electrode demonstrated remarkable capacitance retention of 89% at the end of the cycle, highlighting its robust cycling stability. Furthermore, the EIS spectra with the corresponding equivalent circuit of the BWC-700 electrode before and after cycling studies in the comprehensive cell reveal an R_{ct} value of 0.6 Ω before cycling and it reduced gradually to 0.4 Ω after cycling, indicating commendable capacitance performance and high energy storage capability in supercapacitors, as illustrated in Figure S7, Supporting Information.

The BWC-700 electrode demonstrates a significant energy performance in the acidic 1 M H₂SO₄ framework, with a power density of 556 W kg⁻¹ and a high energy density of 17.15 Wh kg⁻¹ (Figure 5f). Yet with the 3265 W kg⁻¹ high power density, the energy density remains significant at 12.7 Wh kg⁻¹.

This exceptional energy density is clearly illustrated in the Ragone plot, demonstrating that the BWC-700 electrode surpasses documented bio-derived carbon materials in 1 M H₂SO₄, emphasizing its superior energy storage capabilities.

3.5. Electrochemical Evaluation of a Half-Cell in HQ + 1 M H₂SO₄

Ionic liquid electrolytes can exhibit remarkable electrochemical performance, but they are often expensive compared to water-based electrolytes.^[67] An alternate approach is used to increase the device voltage and specific capacitance of electroactive materials, using redox additive electrolytes. Redox additive electrolytes, such as HQ, ferrous ammonium sulfate, potassium iodide, and other redox-based substances, are cost-effective and beneficial when evaluated in water-based 1 M H₂SO₄. In this work, HQ^[68–70] is utilized as a redox additive in 1 M H₂SO₄ due to its less diffusive resistance, strong ionic conductivity, and multiple oxidation and reduction states. The redox mechanism involving HQ and benzoquinone (Q) is responsible for the distinct redox peak observed on the BWC-700 CV curve in 0.01 M HQ/H₂SO₄. When HQ is introduced in small quantities to an H₂SO₄ aqueous electrolyte, it behaves like a redox pair. In the charging process, it undertakes the formation of p-benzoquinone (Q) concerning oxidation, and at a specific discharge process, it reverts to HQ at the specified voltage range.^[71] While the redox behavior of HQ and its derivatives has been well documented in earlier works, this study emphasizes the synergistic enhancement achieved by integrating HQ with a novel one-pot synthesized nitrogen-doped carbon

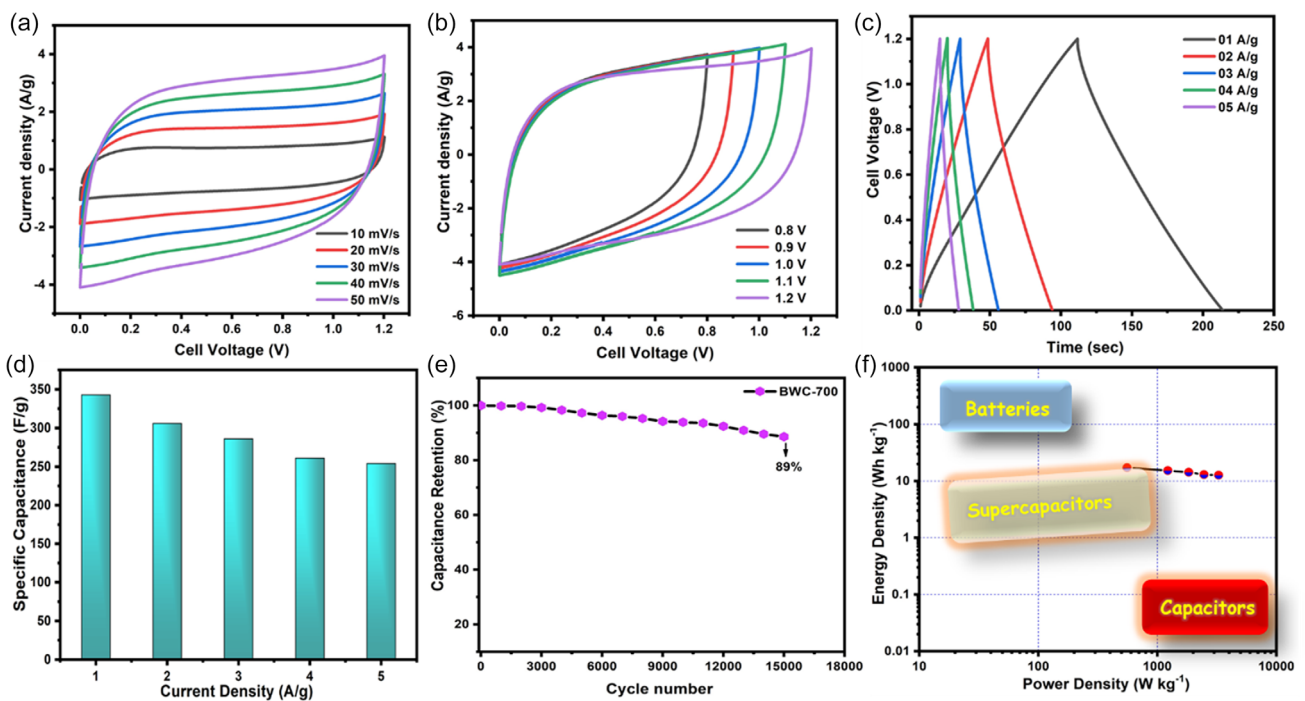


Figure 5. a) CV at various sweep rates, b) CV concerning various potential windows, c) GCD profiles of BWC-700 electrode materials at various current densities, d) specific capacitance plotted against current density, e) cycle stability of BWC-700 at a 5 A g⁻¹ current density, and f) Ragone plot for BWC-700 electrode materials in a two-electrode system in an aqueous 1 M H₂SO₄ electrolyte.

derived from bread waste, offering improved capacitive performance and energy density. The redox process involving HQ transforming into Q with the release of two protons and accepting two electrons promotes reactions that enhance energy storage via pseudocapacitance; the integration of HQ to electrolytes proves beneficial, for enhancing both capacitance and energy storage

capabilities. BWC-700's CV in 1 M H₂SO₄ exhibits a potential window with a quasirectangular shape in the range of -0.8 to 0.4 V, as was previously discussed in the half-cell configuration. This shape typically corresponds to the behavior of an EDLC (**Figure 6a**). Upon addition of HQ redox additive into the electrolyte, the peak current density increases proportionally, causing

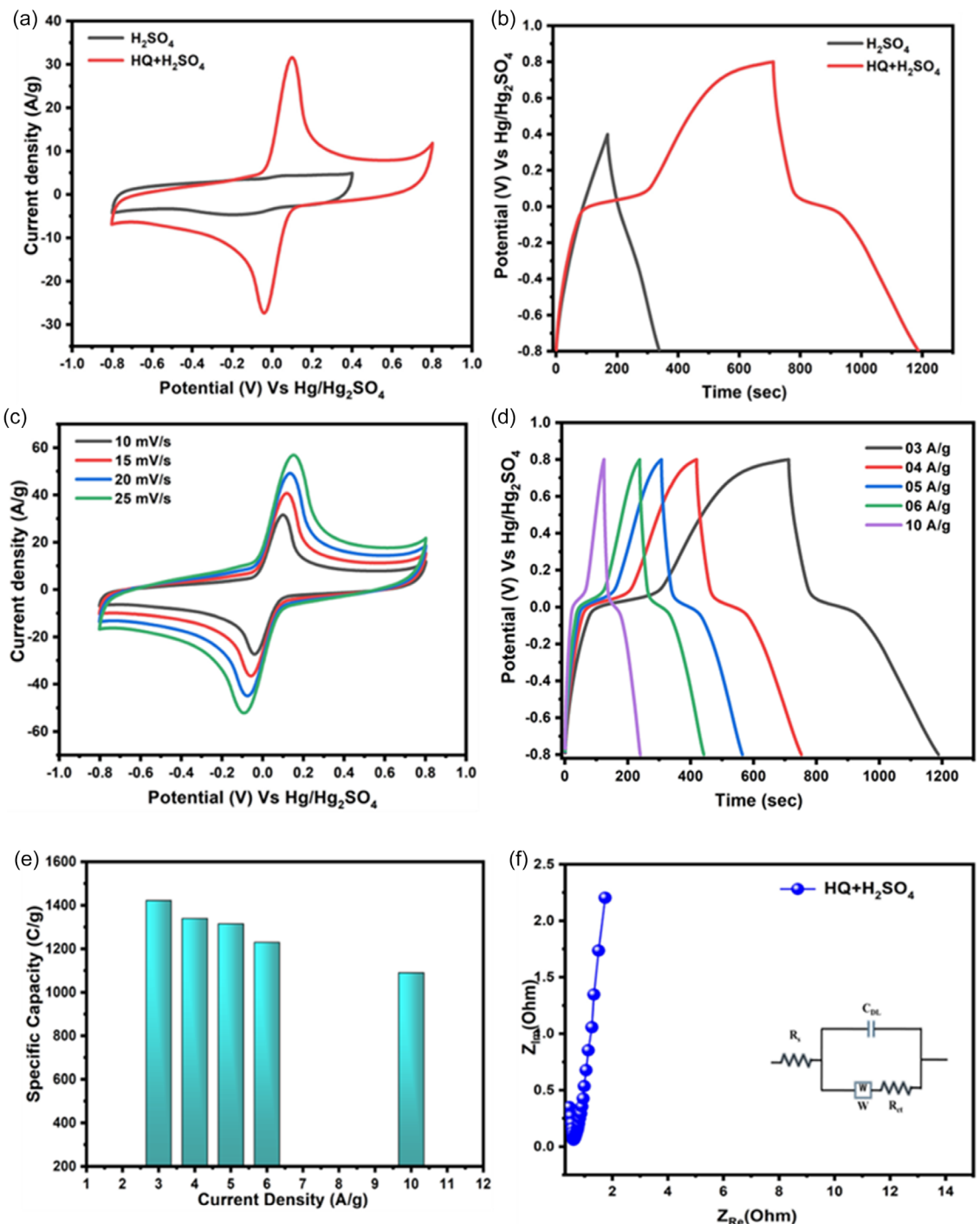


Figure 6. a,b) Depict the CV peak of BWC-700 half cell in 1 M H₂SO₄ and HQ + 1 M H₂SO₄ at a scan rate of 50 mV s⁻¹, with b) further showing the CV profile at a current density of 3 A g⁻¹. c) Illustrates the CV profile under different scan rates using a 1 M H₂SO₄ + KI redox additive electrolyte, while d) presents the CD profile at various current densities under the same conditions. Additionally, e) displays the specific capacitance across different current densities and f) showcases the EIS spectrum of the BWC-700.

the redox potential to shift from -0.8 to $+0.8$ V. This shift becomes apparent with increasing sweep rates, suggesting that HQ redox additive interaction exhibits quasi reversible electrochemical behavior on the carbon matrix. The voltage window undergoes significant alteration, expanding at the range of -0.8 to 0.8 V at various current densities (Figure 6b).

In an aqueous $1\text{ M H}_2\text{SO}_4$ electrolyte, the BWC-700 electrode displays 435 F g^{-1} at a 3 A g^{-1} current density. When 0.01 M of HQ is introduced into a $1\text{ M H}_2\text{SO}_4$ solution, the diffusive characteristics of the redox additive electrolyte gradually enhance the capacity for charge storage, especially due to the distribution of quinone in the electrolyte solution Figure 6c. Therefore, the cell voltage of the electrode is expanded to -0.8 to $+0.8$ V. The CD curve at different current densities ranging from 3 to 10 A g^{-1} is depicted in Figure 6d. It is evident that the current density is significantly increased, resulting in a multiple-fold increase in specific capacity. Figure 6e illustrates that the highest specific capacity, reaching 1422 C g^{-1} , is attained when the current density is 3 A g^{-1} . However, when the current rate escalates to 4 , 5 , 6 , and 10 A g^{-1} , the electrode's capacity diminishes to 1340 , 1315 , 1230 , and 1090 C g^{-1} , respectively, as indicated in Table S2, Supporting Information. The BWC-700 electrode's EIS spectra in the half-cell investigation of $\text{HQ} + 1\text{ M H}_2\text{SO}_4$ reveals an R_{ct} value of 0.57Ω , indicating good performance in terms of specific capacity and high energy storage capacity in supercapacitors (Figure 6f).

3.6. Two-Electrode Cell in $\text{HQ} + 1\text{ M H}_2\text{SO}_4$

The Trasatti technique is employed for assessing the proportion of capacitive and diffusive contributions in energy storage applications across the working electrodes.^[72] In $1\text{ M H}_2\text{SO}_4$, the relationship between the scan rate ($v^{1/2}$ and $v^{-1/2}$) and specific capacity offers insights into the charge storage mechanism, evaluating the contributions of EDLC and PC (Figure S8a,b, Supporting Information). Furthermore, Figure S8c,d, Supporting Information presents a graph showing the inverse of specific capacity plotted against the square root of the scan rate. Additionally, there are graphs illustrating the relationship between specific capacity and the reciprocal of the square root of the scan rate. These measurements were taken in an electrolyte containing $1\text{ M H}_2\text{SO}_4$ with HQ redox additive. In $1\text{ M H}_2\text{SO}_4$, electrodes based on BWC-700 demonstrate a 77% contribution from EDLC represented by the red portion, and a 23% contribution from PC indicated by the blue segment, as depicted in Figure S8e, Supporting Information. Nevertheless, a notable alteration is evident with the introduction of redox-active components utilizing $0.01\text{ M HQ} + 1\text{ M H}_2\text{SO}_4$ as the electrolyte. Here, the contributions from EDLC and PC are 33% and 67%, respectively. This substantial enhancement in specific capacity with 0.01 M HQ suggests a significant involvement of faradaic capacitance stemming from the redox additive. Furthermore, similar electrochemical performance was noted in the symmetrical cell utilizing a two-electrode setup at a device voltage of 1.8 V, with the inclusion of HQ redox additive into the $1\text{ M H}_2\text{SO}_4$ solution. The CV peak displayed a characteristic rectangular shape with

diminished pseudocapacitive behavior, indicating resemblances in the redox reaction occurring within the BWC-700 material (Figure 7a). The energy efficiency and coulombic efficiency of the electrode material after incorporating HQ redox additive was clearly explained in the Supporting Information.

A nonlinear GCD profile is shown in Figure 7b as a consequence of adding 0.01 M HQ redox additive to the $1\text{ M H}_2\text{SO}_4$ aqueous electrolyte. This GCD profile showcases an improved cell voltage and prolonged GCD duration, attributed to the existence of surface redox moieties present within the aqueous electrolyte. The redox characteristics are perceived at 1.8 V voltage, leading to redox reactions between the two electrodes. The BWC-700 sample exhibits an optimal specific capacity of 904 C g^{-1} at a current density of 2 A g^{-1} with the incorporation of the HQ redox agent in $1\text{ M H}_2\text{SO}_4$. However, with increased current densities of 3 , 4 , and 5 A g^{-1} , there is a steady reduction in capacity to 840 , 720 , and 640 C g^{-1} , respectively (Figure 7c). The upper limit of specific capacity is noted for BWC-700 in the redox-active electrolyte ($\text{HQ} + 1\text{ M H}_2\text{SO}_4$). The heightened electrochemical performance can be attributed to the redox nature of HQ, confirming that BWC-700 can be a promising electrode material for supercapacitor devices with an $\text{HQ} + 1\text{ M H}_2\text{SO}_4$ electrolyte.

Figure 7d demonstrates that BWC-700 exhibits exceptional long-term cycle stability, with a retention rate of 82% after 5000 CD cycles. Energy and power density are vital parameters employed to evaluate the performance of the supercapacitor. The morphology of before and after cycling of the BWC-700 electrodes underwent analysis utilizing FE-SEM (Figure S9a,b, Supporting Information), following 5000 cycles, the electrode surface exhibited cracks attributed to volumetric variations during charge and discharge cycles. Notably, the porous morphology of the material endured unaltered during cycling. This observation accentuates the remarkable capacity of BWC-700 to withstand volumetric changes throughout the cycling process is outstanding for supercapacitor application. A Ragone plot presented in Figure 7e illustrates high-energy-density (56.5 Wh kg^{-1}) and high-power density (4363 W kg^{-1}). These values indicate a 3.3 times escalated performance of high energy compared to that in aqueous electrolytes. Figure 7f provides a comparison with similar work related to redox electrolytes, and Table S3, Supporting Information compares the present study with recent reports on redox-active agents and dual redox-active agents used for supercapacitors. The discussed aspects, along with a facile and economic approach, have attracted the attention of researchers and stakeholders to explore redox-active electrolytes for supercapacitors. While redox enhancers, like HQ are commonly proven to boost capacitance in half cell setups, their efficiency in two electrode systems is often doubted due to issues, like restricted redox species diffusion or issues with stability and long-term performance retention during cycling processes. Based on our results the consistent and impressive performance shows that HQ can be a redox additive, in real world supercapacitor uses when paired with carbon design and electrolyte enhancements.

Dunn's technique, on the other hand, provides information regarding the (k_1v) and the diffusion-capacitance factor ($k_2v^{1/2}$) by analyzing the CV through Equation (1) and (2)^[73]

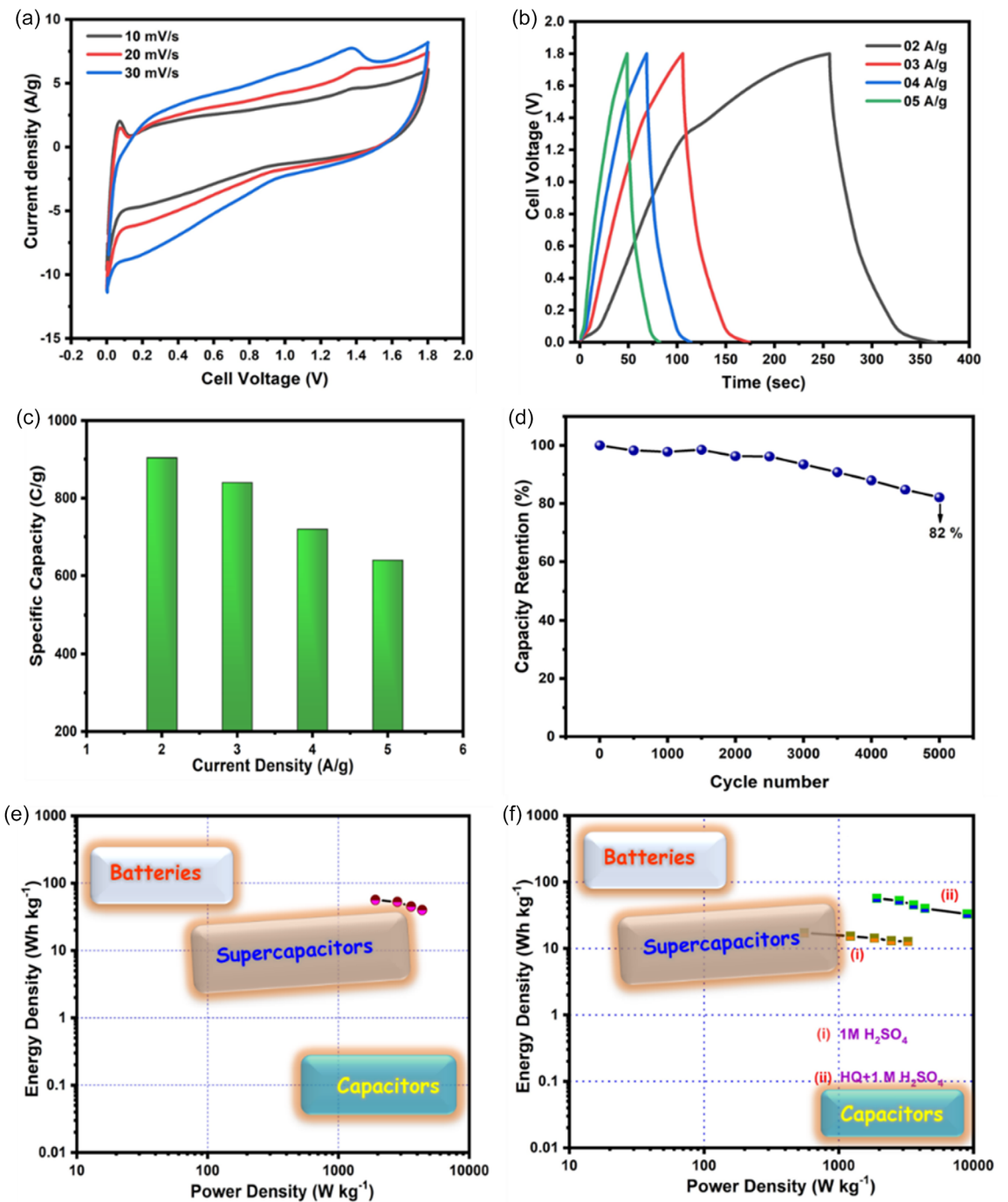


Figure 7. Displays various aspects of the BWC-700 symmetric cell in HQ + 1 M H₂SO₄ electrolyte: a) The CV profile, b) GCD profile, c) specific capacity versus various current densities, d) BWC-700 long cyclability studies at a current rate of 5 A g⁻¹, e) BWC-700 Ragone plot using HQ + 1 M H₂SO₄, and f) comparison of a Ragone plot for all electrolytes used.

$$i(V) = k_1 v + k_2 v^{1/2} \quad (1)$$

$$i(V)/v^{1/2} = k_1 v^{1/2} + k_2 \quad (2)$$

The purpose of this method was to evaluate the surface and diffusion-controlled contributions of BWC-700 in redox additive electrolytes under varying scan rates. In this equation, V stands for voltage, v stands for scan rate, and k_1 and k_2 are constants

that denote surface capacitive and diffusion-controlled contributions, respectively. **Figure 8a-d** presents the CVs of BWC-700 in HQ + 1 M H₂SO₄ electrolyte, delineating surface and diffusion-capacitance contributions. The CVs reveal that with an increase in sweep rate, the diffusion contribution diminishes, whereas the surface contribution escalates. At sweep rates of 10, 15, 20, and 25 mV s⁻¹, BWC-700 displayed capacitive-controlled contributions of 33%, 36%, and 40%, respectively,

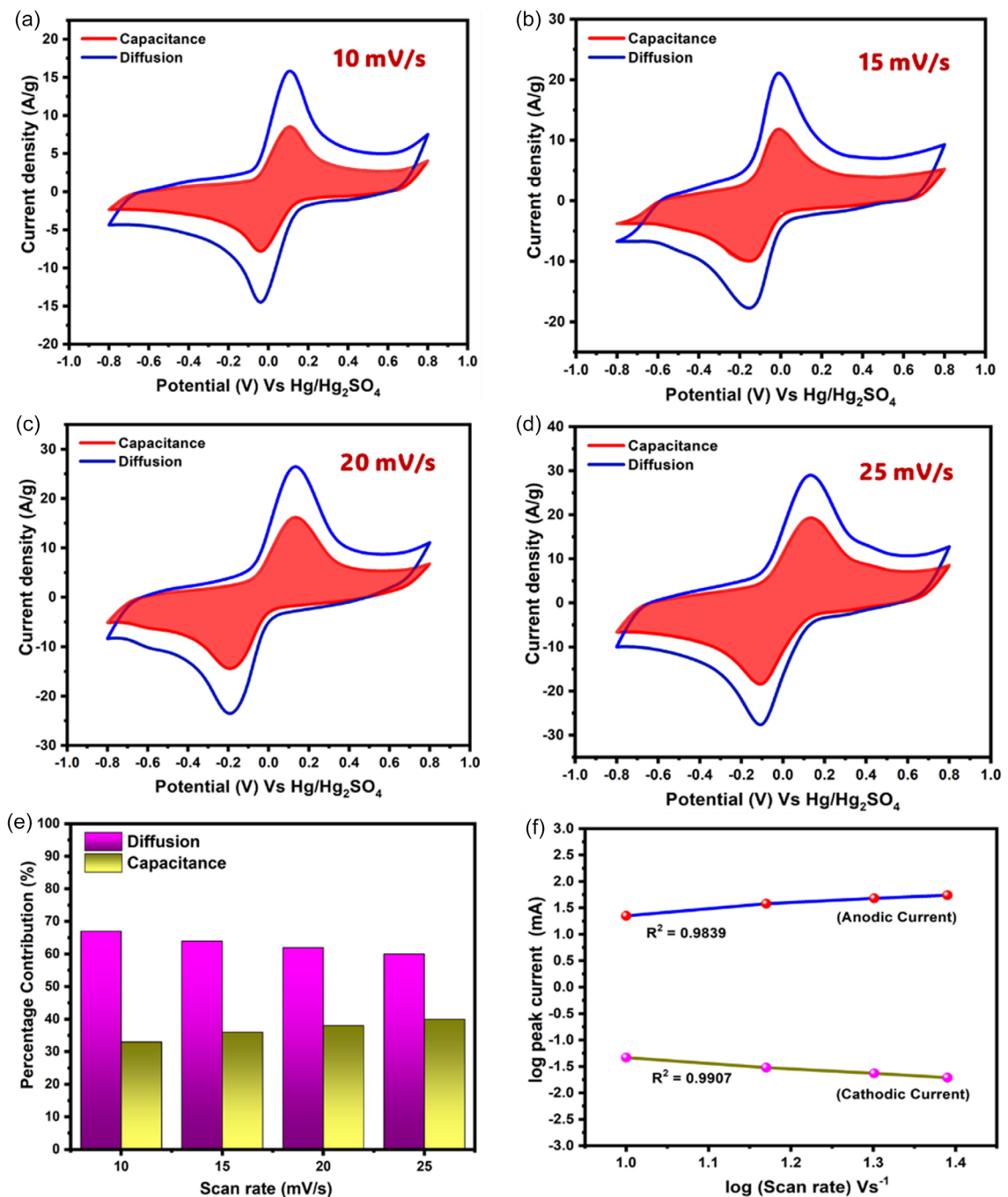


Figure 8. a-d) Comparison of diffusion and capacitive contribution of BWC-700 symmetric cell in HQ + 1 M H₂SO₄, at various scan rates, e) diffusion and capacitive contribution ratio of BWC-700 in HQ + 1 M H₂SO₄ and f) anodic and cathodic peak current linear fit with respect to log scan rate.

in Figure 8e. This shows that ions impact the capacitive behavior, leading to a decrease in the utilization of effective surface areas for charge storage at higher scan rates. Upon the addition of the redox additive, the diffusive process becomes the predominant factor, indicating rapid charge transfer kinetics as well as outstanding rate capability of the electrode, primarily pseudocapacitive behavior. It also demonstrates diffusive-controlled contributions of 67%, 64%, 62%, and 60% for BWC-700 at 10, 15, 20, and 25 mV s⁻¹ scan rates, respectively.

Moreover, a current associated with surface reaction-controlled processes in Dunn's plot Figure 8f was assessed utilizing the values of K_1 and K_2 . The BWC-700 electrode exhibited contributions to surface-reaction capacitive and diffusive energy, aligning with the results obtained through Dunn's approach.^[74,75] High-rate capacitance performance is facilitated by faster electron transfer and a larger exposed active surface area, with R^2 values for anodic and cathodic currents of 0.9839 and 0.9907, respectively.

Table S3, Supporting Information these findings indicate that despite recent investigations into a range of redox-based electrolytes and porous carbon materials to assess the energy storage performance in both half-cell and full-cell configurations, AC obtained from bread biomass waste (BWC-700) exhibits superior energy properties compared to alternative electrode materials discussed in prior studies. This discovery implies that utilizing BWC-700 bio-carbon could present a significant benefit in terms of energy efficiency for supercapacitors. The remarkable superiority of BWC-700 implies that integrating this bio-carbon into supercapacitors could result in a decrease in the overall cost of electrode materials for commercially available supercapacitors. This potential cost reduction, combined with superior performance, positions BWC-700 as a promising and economically beneficial material for advancing the practical application of supercapacitors across various industries.

4. Conclusions

An effective single step chemical activation process was used to create nitrogen-doped porous carbon from biomass leftover from discarded bread. FE-SEM revealed the resulting AC with a highly porous nature and irregular surface morphology. Among the various carbons synthesized, BWC-700 exhibited exceptional performance across aqueous and redox-based electrolytes. The activated porous carbon has a significantly substantial specific surface area, which greatly enhances its electrochemical characteristics. In a three-electrode supercapacitor setup, it demonstrated a specific capacitance of 486 F g^{-1} at 1 A g^{-1} current density and 1422 C g^{-1} at a 3 A g^{-1} current rate in both $1 \text{ M H}_2\text{SO}_4$ and $\text{HQ} + 1 \text{ M H}_2\text{SO}_4$ electrolytes. In a two-electrode cell setup, the cell exhibits an exceptional specific capacitance of 343 F g^{-1} in a $1 \text{ M H}_2\text{SO}_4$ solution, and 904 C g^{-1} in a 0.01 M HQ integrated $1 \text{ M H}_2\text{SO}_4$ electrolyte. Remarkably, a substantial enhancement in specific energy was observed, reaching 17.15 Wh kg^{-1} in aqueous electrolytes and 56.5 Wh kg^{-1} in redox additive-containing electrolytes. These findings highlight the potential of utilizing bread biomass waste as a sustainable precursor for producing porous carbon materials suitable for high-performance supercapacitor applications.

Associated Content

Electronic supplementary information (ESI) is available: The ESI contains the materials and electrochemical properties of BWC-700 electrode material, including FT-IR spectrum analysis, cyclic voltammetry (CV), galvanostatic charge-discharge (GCD) analysis of both bare carbon and BWC-700 electrode materials, FE-SEM images of BWC-800 & BWC-900, and determination of C_{sp} of BWC-700 without Urea, and the Trasatti Analysis detailed explanation. For detailed information, refer to the provided <https://doi.org/10.1002/batt.202500342>.

Acknowledgements

The authors would like to gratefully acknowledge the necessary support provided by the Interdisciplinary Research Center for Construction and Building Materials (IRC-CBM) at King Fahd University of Petroleum & Minerals (KFUPM), Dhahran, Saudi Arabia. K.M. thanks KFUPM, Saudi Arabia for the postdoctoral fellowship.

Conflict of Interest

The authors declare no conflict of interest.

Data Availability Statement

The data that support the findings of this study are available on request from the corresponding author. The data are not publicly available due to privacy or ethical restrictions.

Keywords: chemical activation • porous structure • redox-active • supercapacitors • wheat bread waste

- [1] P. Manasa, Z. J. Lei, F. Ran, *J. Energy Storage* **2020**, *30*, 101494.
- [2] M. Shetty, K. Manickavasakam, C. Sabbanahalli, C. Bekal, I. I. Misnon, P. A. Subrahmanyam, K. Roy, P. D. Shivaramu, B. S. Shenoy, D. Rangappa, *J. Energy Storage* **2023**, *72*, 108116.
- [3] Z. Zhu, T. Jiang, M. Ali, Y. Meng, Y. Jin, Y. Cui, W. Chen, *Chem. Rev.* **2022**, *122*, 16610.
- [4] W. Chen, C. Xia, R. B. Rakhi, H. N. Alshareef, *J. Power Sources* **2014**, *267*, 521.
- [5] T. Ahmad, Z. Zhu, M. Sajid, W. Wang, Y. Ma, M. Ali, N. A. Khan, S. Liu, Z. Zhang, W. Chen, *Int. J. Miner., Metall. Mater.* **2025**, *32*, 1461.
- [6] Z. Zhu, Z. Liu, Y. Yin, Y. Yuan, Y. Meng, T. Jiang, Q. Peng, W. Wang, W. Chen, *Nat. Commun.* **2022**, *13*, 2805.
- [7] K. Rajendran, K. Lolupiman, M. Okhawilai, S. K. Helen Annal Therese, P. Tan, J. Qin, *J. Alloys Compd.* **2024**, *980*, 173549.
- [8] R. N. Shaker, S. Mohammed, Y. A. Abdulsayed, *J. Met., Mater. Miner.* **2023**, *33*, 1791.
- [9] B. Shaku, T. P. Mofokeng, N. J. Coville, K. I. Ozoemena, M. S. Maubane-Nkadieng, *Electrochim. Acta* **2023**, *442*, 141828.
- [10] D. Zhang, J. Cao, X. Zhang, Z. Zeng, N. Insin, J. Qin, Y. Huang, *Adv. Energy Sustainability Res.* **2022**, *3*, 2100183.
- [11] K. Thongkam, N. Chaiyut, M. Panapoy, B. Ksapabutr, *J. Met., Mater. Miner.* **2023**, *33*, 1.
- [12] N. Keawploy, R. Venkatkarthick, P. Wangyao, X. Zhang, R. Liu, J. Qin, *Energy Fuels* **2020**, *34*, 8977.
- [13] B. R. Sankapal, H. B. Gajare, S. S. Karade, D. P. Dubal, *RSC Adv.* **2015**, *5*, 48426.
- [14] B. Sankapal, C. Lokhande, *Mater. Chem. Phys.* **2002**, *74*, 126.
- [15] R. Çetin, M. Kaya, M. Akdemir, M. A. Arserim, S. Abut, *Int. J. Hydrogen Energy* **2024**, *52*, 1261.
- [16] R. Venkatkarthick, J. Qin, *Environ. Technol. Innov.* **2021**, *22*, 101474.
- [17] M. M. Taha, L. G. Ghanem, M. A. Hamza, N. K. Allam, *ACS Appl. Energy Mater.* **2021**, *4*, 10344.
- [18] E. Elanthamilan, B. Sriram, S. Rajkumar, C. Dhaneshwaran, N. Nagaraj, J. P. Merlin, A. Vijayan, S. F. Wang, *Mater. Res. Bull.* **2019**, *112*, 390.
- [19] S. S. Raut, B. R. Sankapal, M. S. A. Hossain, S. Pradhan, R. R. Salunkhe, Y. Yamauchi, *Eur. J. Inorg. Chem.* **2018**, *2018*, 137.
- [20] R. Sun, H. Li, Y. Chen, G. Xie, R. Yang, C. Yang, *Colloids Surf., A.* **2024**, *683*, 132978.
- [21] S. Zhang, P. Dai, H. Liu, L. Yan, H. Song, D. Liu, X. Zhao, *ACS Appl. Energy Mater.* **2020**, *3*, 12627.
- [22] E. Elanthamilan, S. Rajkumar, J. P. Merlin, D. S. Jona, K. Monisha, B. C. Meena, *Electrochim. Acta* **2020**, *359*, 136953.

- [23] N. Boonraksa, E. Swatsitang, K. Wongsaprom, *Mater. Sci. Eng. B* **2024**, 301, 117151.
- [24] S. Zhong, L. Dai, H. Xu, C. Yuan, S. Wang, *Diamond Relat. Mater.* **2024**, 141, 110714.
- [25] N. Boulanger, A. V. Talyzin, S. Xiong, M. Hultberg, A. Grimm, *Colloids Surf. A* **2024**, 680, 132684.
- [26] K. D. Verma, P. Sinha, M. K. Ghorai, K. K. Kar, *Diamond Relat. Mater.* **2022**, 123, 108879.
- [27] S. Yaglikci, Y. Gokce, E. Yagmur, Z. Aktas, *Environ. Technol. (United Kingdom)* **2020**, 41, 36.
- [28] D. Alvira, D. Antorán, J. J. Manyà, *Chem. Eng. J.* **2022**, 447, 137468.
- [29] R. Srinivasan, E. Elaiyappillai, H. P. Pandian, R. Vengudusamy, P. M. Johnson, S. M. Chen, R. Karvembu, *J. Electroanal. Chem.* **2019**, 849, 11382.
- [30] Y. Gao, L. Li, Y. Jin, Y. Wang, C. Yuan, Y. Wei, G. Chen, J. Ge, H. Lu, *Appl. Energy* **2015**, 153, 41.
- [31] N. Sudhan, K. Subramani, M. Karnan, N. Ilayaraja, M. Sathish, *Energy Fuels* **2017**, 31, 977.
- [32] M. Karnan, A. G. K. Raj, K. Subramani, S. Santhoshkumar, M. Sathish, *Sustainable Energy Fuels* **2020**, 4, 3029.
- [33] M. Karnan, K. Subramani, N. Sudhan, N. Ilayaraja, M. Sathish, *ACS Appl. Mater. Interfaces* **2016**, 8, 35191.
- [34] M. Karnan, K. Subramani, P. K. Srividhya, M. Sathish, *Electrochim. Acta* **2017**, 228, 586.
- [35] L. Sun, C. Tian, M. Li, X. Meng, L. Wang, R. Wang, J. Yin, H. Fu, *J. Mater. Chem. A* **2013**, 1, 6462.
- [36] L. Zhang, T. You, T. Zhou, X. Zhou, F. Xu, *ACS Appl. Mater. Interfaces* **2016**, 8, 13918.
- [37] K. Subramani, N. Sudhan, M. Karnan, M. Sathish, *ChemistrySelect* **2017**, 2, 11384.
- [38] R. Mehdi, S. R. Naqvi, A. H. Khoja, R. Hussain, *Fuel* **2023**, 348, 128529.
- [39] G. Dhakal, D. R. Kumar, S. Sahoo, J. J. Shim, *Carbon N. Y.* **2023**, 208, 277.
- [40] M. Karnan, K. H. Prakash, S. Badhulika, *J. Energy Storage* **2022**, 53, 105189.
- [41] P. Numee, T. Sangtawesin, M. Yilmaz, K. Kanjana, *Carbon Resour. Convers.* **2023**, 7, 100192.
- [42] D. Wu, T. Wang, L. Wang, D. Jia, *Microporous Mesoporous Mater.* **2019**, 290, 109556.
- [43] D. Wang, G. Fang, T. Xue, J. Ma, G. Geng, *J. Power Sources* **2016**, 307, 401.
- [44] J. Yang, J. Peng, Y. Lei, Y. Tang, P. Liu, J. Zeng, C. Yi, Y. Shen, L. Zheng, X. Wang, *ACS Appl. Energy Mater.* **2024**, 7, 469.
- [45] P. Hepsi, S. Rajkumar, E. Elanthamilan, S. F. Wang, J. P. Merlin, *New J. Chem.* **2022**, 46, 8863.
- [46] E. Huarote-Garcia, A. A. Cardenas-Riojas, I. E. Monje, E. O. López, O. M. Arias-Pinedo, G. A. Planes, A. M. Baena-Moncada, *ACS Environ. Au* **2024**, 4, 80.
- [47] S. Anand, M. W. Ahmad, A. Syed, A. H. Bahkali, M. Verma, B. H. Kim, A. Choudhury, *J. Ind. Eng. Chem.* **2024**, 129, 309.
- [48] A. Andooz, E. Kowsari, M. D. Najafi, A. Chinnappan, M. A. Eshlaghi, S. Ramakrishna, *Electrochim. Acta* **2024**, 477, 143773.
- [49] M. Wang, H. Liu, D. D. Zhai, X. Y. Chen, Z. J. Zhang, *J. Power Sources* **2019**, 416, 79.
- [50] B. Tiwari, A. Joshi, M. Munjal, G. Kaur, R. K. Sharma, G. Singh, *J. Phys. Chem. Solids* **2022**, 161, 110449.
- [51] L. F. Aval, M. Ghoranneviss, G. B. Pour, *Heliyon* **2018**, 4, e00862.
- [52] S. Qu, J. Wan, C. Dai, T. Jin, F. Ma, *J. Alloys Compd.* **2018**, 751, 107.
- [53] J. Fang, X. Zhang, X. Miao, Y. Liu, S. Chen, Y. Chen, J. Cheng, W. Wang, Y. Zhang, *Electrochim. Acta* **2018**, 273, 495.
- [54] R. Samantray, M. Karnan, K. S. Vivekanand, C. J. Anjeline, S. C. Mishra, M. Sathish, *Sustainable Energy Fuels* **2021**, 5, 518.
- [55] G. Hariharan, S. Arunpandiyan, V. Shanmugapriya, S. Bharathi, M. Babu, B. Selvakumar, A. Arivarasan, *J. Energy Storage* **2023**, 57, 106178.
- [56] L. Dou, S. Zhou, J. Ma, C. Zhao, P. Cui, S. Ye, P. Feng, X. Gu, S. Huang, X. Tao, *J. Mater. Chem. C* **2024**, 12, 521.
- [57] S. A. Sawant, M. R. Waikar, G. R. Chodankar, S. R. Gurav, A. V. Patil, R. S. Vhatkar, R. G. Sonkawade, *J. Energy Storage* **2024**, 76, 109739.
- [58] X. Zheng, Z. L. Lei, J. R. Wang, Q. F. Lü, *Biomass Bioenergy* **2024**, 181, 107063.
- [59] G. Qin, C. Wu, X. Song, W. He, J. Yang, X. Yu, Q. Chen, *Fuel* **2024**, 357, 130033.
- [60] B. Krüner, J. Lee, N. Jäckel, A. Tolosa, V. Presser, *ACS Appl. Mater. Interfaces* **2016**, 8, 9104.
- [61] G. Zhao, L. Shi, J. Xu, X. Yan, T. S. Zhao, *Int. J. Hydrogen Energy* **2018**, 43, 1470.
- [62] S. T. Senthilkumar, R. K. Selvan, J. S. Melo, C. Sanjeeviraja, *ACS Appl. Mater. Interfaces* **2013**, 5, 10541.
- [63] K. Subramani, S. Shunmugasundaram, V. Duraisamy, R. Ilavarasi, S. M. S. Kumar, M. Sathish, *J. Colloid Interface Sci.* **2022**, 606, 286.
- [64] L. Yan, D. Li, T. Yan, G. Chen, L. Shi, Z. An, D. Zhang, *ACS Appl. Mater. Interfaces* **2018**, 10, 42494.
- [65] X. Zheng, L. Miao, Z. Song, W. Du, D. Zhu, Y. Lv, L. Li, L. Gan, M. Liu, *J. Mater. Chem. A* **2022**, 10, 611.
- [66] L. Niu, C. Shen, L. Yan, J. Zhang, Y. Lin, Y. Gong, C. Li, C. Q. Sun, S. Xu, *J. Colloid Interface Sci.* **2019**, 547, 92.
- [67] R. Chen, D. Bresser, M. Saraf, P. Gerlach, A. Balducci, S. Kunz, D. Schröder, S. Passerini, J. Chen, *ChemSusChem* **2020**, 13, 2205.
- [68] N. Yadav, N. Yadav, S. A. Hashmi, *J. Power Sources* **2020**, 451, 227771.
- [69] K. Manickavasakam, S. S. Balaji, S. Kaipannan, A. G. K. Raj, S. Veeman, S. Marappan, *J. Energy Storage* **2020**, 32, 101939.
- [70] M. Sandhiya, S. S. Balaji, M. Sathish, *Energy Fuels* **2020**, 34, 11536.
- [71] S. Roldán, C. Blanco, M. Granda, R. Menéndez, R. Santamaría, *Angew. Chem., Int. Ed.* **2011**, 50, 1699.
- [72] J. Zhi, O. Reiser, F. Huang, *ACS Appl. Mater. Interfaces* **2016**, 8, 8452.
- [73] D. Govindarajan, K. Kirubahanan, M. Selvaraj, A. Sanni, J. Theerthagiri, M. Y. Choi, S. Kheawhom, *Appl. Surf. Sci.* **2023**, 630, 157475.
- [74] T. Li, Z. Liu, L. Zhu, F. Dai, L. Hu, L. Zhang, Z. Wen, Y. Wu, *J. Mater. Sci.* **2018**, 53, 16458.
- [75] Y. Fang, X. Chen, C. Yin, L. Cui, *Ceram. Int.* **2021**, 47, 24973.

Manuscript received: May 6, 2025

Revised manuscript received: June 30, 2025

Version of record online: